Achieving 17.7% Efficiency of Ternary Organic Solar Cells by Incorporating a High Lowest Unoccupied Molecular Orbital Level and Miscible Third Component

*Alfonsina Abat Amelenan Torimtubun, Maria Méndez, Enas Moustafa, Josep Pallarès, Emilio Palomares, and Lluis F. Marsal**

A ternary strategy has been demonstrated as being an effective method to improve the power conversion efficiency (PCE); however, general rules for materials selection are not fully comprehended. Herein, nonfullerene acceptor ITIC-M and fullerene acceptor $PC_{70}BM$ possessing higher lowest unoccupied molecular orbital (LUMO) and good miscibility with nonfullerene acceptor Y7 are incorporated as third components in the state-of-the-art of PM6:Y7 binary blend. As a result, the device PCE for both ternary devices improves from 16.46% for binary host to 17.73% and 17.67% for ITIC-M- and $PC_{70}BM$-based ternary devices, respectively. The higher LUMO of the guest acceptor can play multiple roles to elevate the open-circuit voltage such as reducing energy-loss and reverse saturation current, creating less-localized shallow trap sites along with suppressing charge recombination, and decreasing Urbach energy. Moreover, the good miscibility facilitates an alloy-like phase in acceptors domain for efficient exciton dissociation and electron transport, which leads to improved short-circuit current density and fill factor in ternary devices. The results provide a promising approach to realize high-performance ternary organic solar cells by synergizing the compatible third component with host acceptor.

1. Introduction

The bulk-heterojunction organic solar cells (OSCs) have made significant progress thanks to the synergistic advances in materials design and device engineering, boosting the power conversion efficiency (PCE) to over 18% in single-junction OSCs.[1–4] The recent emergence of high-performance Y-series nonfullerene acceptors (NFAs) paired with polymer donor PM6 has motivated a major revolution in OSCs field. To further boost PCE of OSCs, constructing ternary organic solar cells (TOSCs) is a facile and effective approach via introducing third component, either a secondary donor or a secondary acceptor, in binary host blend. The third component in TOSCs can have various functions for successfully constructing efficient TOSCs such as widening the absorption spectra, modulating the energetics, regulating morphology, and enhancing stability,[5–10] making a rational selection of third component material is of urgent and fundamental importance.

To choose a compatible third component, some key factors must be considered, mainly from the electrical and morphological perspectives. Considering the energetic perspective, a higher energy lowest unoccupied molecular orbital (LUMO) material for a two acceptors system or a deeper highest occupied molecular orbital (HOMO) material for a two donors system was selected as third component to increase simultaneously the open-circuit voltage (V_{OC}) and short-circuit current density (J_{SC}) values of ternary device.[11–13] In the case of two acceptors system, either fullerene acceptor (FA) or NFA can be selected as a good ternary composite in the state-of-the-art PM6:Y-derivative binary blend system, depending on its compatibility with Y-derivative host acceptor. For example, Zhang and co-workers introduced an amorphous ICBA into PM6:Y7 binary blend, which helps improve the V_{OC} by elevating the LUMO energy levels and concurrently increase J_{SC} by extending the absorption in a short wavelength band, thus boosting the PCEs of the corresponding TOSCs to 16.76%.[14] In fact, employing a NFA as third component with a smaller bandgap and a higher LUMO energy level than the acceptor host can achieve simultaneously enhancement in both V_{OC} and J_{SC}, as demonstrated by An's group by adding MF1 in PM6:Y6 binary system achieving a high PCE of 17.22%.[15]

On the morphological perspective, from the thermodynamic point of view, it has been demonstrated that a third component

A. A. A. Torimtubun, E. Moustafa, J. Pallarès, L. F. Marsal
Department of Electric
Electronic and Automatic Engineering
Universitat Rovira i Virgili
Avda. Països Catalans 26, 43007 Tarragona, Spain
E-mail: lluis.marsal@urv.cat

M. Méndez, E. Palomares
Institute of Chemical Research of Catalonia (ICIQ-BIST)
Av. Països Catalans 16, 43007 Tarragona, Spain

E. Palomares
ICREA
Passeig Lluís Companys 23, 08010 Barcelona, Spain

The ORCID identification number(s) for the author(s) of this article can be found under https://doi.org/10.1002/solr.202300228.

DOI: 10.1002/solr.202300228

with suitable miscibility with host acceptor is more likely to form a mixed acceptor phase, resulting in quasilinear relationship between open-circuit voltage (V_{OC}) and weight ratio of third component. Jia et al. found that by adding ITIC as third component into PM6:Y6 binary blend, the variations of ITIC content in acceptor domain can linearly tune V_{OC}, which was modulated by the interplay between CT states and nonradiative recombination rates.[16] Furthermore, structural similarities between two nonfullerene acceptors allow them to form an alloy-like composite with homogeneous acceptor phases, leading to optimize energy-level alignment and maintain the blend morphology, thus maintaining the device fill factor (FF).[17] Apart from the performance enhancement, achieving stable TOSCs is critical for commercialization, thus Dong and co-workers reported that similar structure of two NFAs could facilitate better thermal and photostability of TOSCs, which might be associated with suppressed aggregation tendency by alloy formation.[18] These studies highlight the synergizing use of third component that has a higher LUMO level and a relatively low miscibility with the host acceptor for obtaining highly efficient NFA-based TOSCs. However, reports of highly efficient TOSCs with acceptor alloy-like formation are still rare, especially for Y7-based systems.

In this contribution, two distinct categories of acceptor materials—the classic fullerene derivative $PC_{70}BM$ and the classic nonfullerene ITIC-M—are employed as the third components in the state-of-the-art PM6:Y7 host binary system. Despite the fact that the two acceptor guests $PC_{70}BM$ and ITIC-M possess completely different chemical structures, we notice a PCE enhancement in the ternary devices due to their good miscibility and higher LUMO energy level relative to the host acceptor Y7. Compared to the champion PCE of the PM6:Y7 binary OSCs (PCE = 16.46%), the champion PCEs of the ternary devices as high as 17.73% and 17.67% for PM6:Y7:ITIC-M and PM6:Y7:$PC_{70}BM$ blends, respectively, are demonstrated. Due to the good compatibility between ITIC-M or $PC_{70}BM$ and Y7, an acceptor alloy-like state was formed, showing a nondisrupted bicontinous film morphology in ternary blends, which is favorable for charge dissociation, charge collection, and transport properties with suppressed bimolecular and trap-assisted charge recombination. The higher LUMO levels of the third components help the ternary OSCs elevate the V_{OC} by reducing energy-loss and reverse saturation current, creating less-localized shallow trap sites along with suppressing charge recombination and Urbach energy. Furthermore, photoluminescence and single material device investigations demonstrate energy transfer between the two well-mixed acceptors, contributing to the increased current. The combination of these improvements leads in a simultaneously enhanced V_{OC}, J_{SC}, and FF with respect to those of binary host. The findings imply that one of the keys to obtain high-efficiency ternary OSCs is by establishing good morphological compatibility with host materials with suitable energy levels and complementary absorption.

2. Results and Discussion

Figure 1a depicts the chemical structures of host donor PM6, host NFA-based Y7, and third components NFA-based ITIC-M and FA-based $PC_{70}BM$, as well as the schematic illustration of the device structure used in this work. Figure 1b shows the HOMO and LUMO energy levels of PM6, Y7, ITIC-M, and $PC_{70}BM$, which are consistent with previous studies.[17,19–21] Both of secondary acceptors $PC_{70}BM$ and ITIC-M exhibit higher lying LUMO levels compared to those of host acceptor Y7, which is expected to help increase V_{OC} values in the ternary OSCs. Figure 1c presents the normalized UV–vis absorption spectra of the used materials in their neat-film states. The maximum

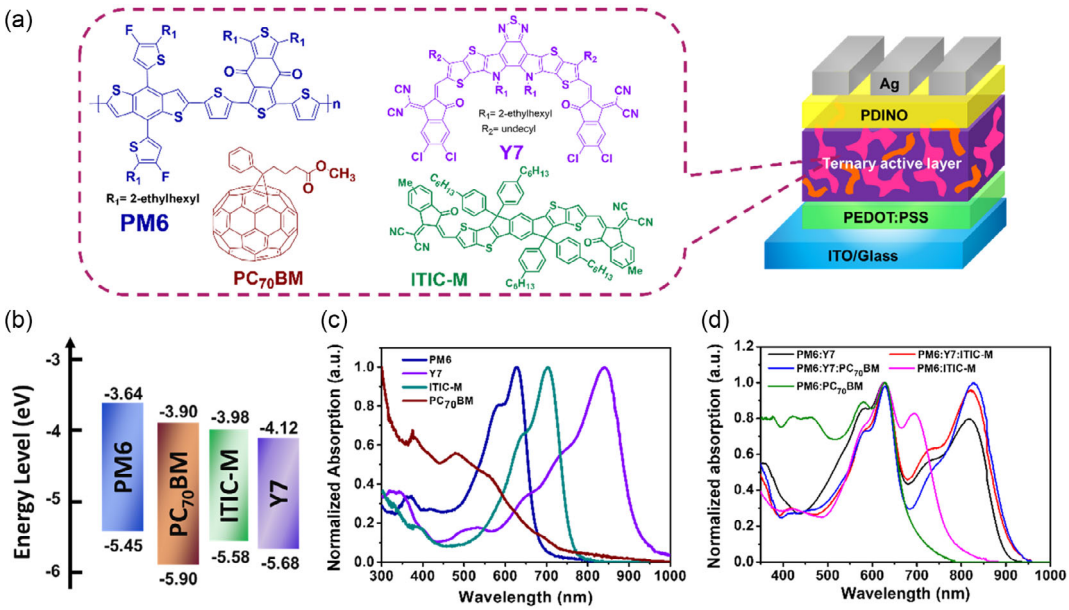

Figure 1. a) Chemical structures of photoactive materials and schematic diagram of device architecture used in this study, b) energy-level diagrams of PM6, Y7, ITIC-M and $PC_{70}BM$, c) normalized UV–vis absorption spectra of neat PM6, Y7, ITIC-M, and $PC_{70}BM$ films; and d) normalized absorption spectra of the binary and ternary blend films.

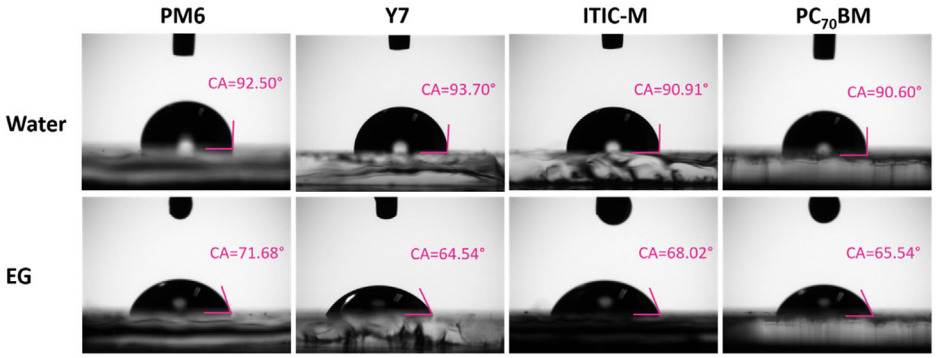

Figure 2. Contact angle images of the neat films of PM6, Y7, ITIC-M, and $PC_{70}BM$. The values of the images are the average contact angle from nine tests through different parts in the same film.

absorption peaks of ITIC-M (703 nm) lie between those of PM6 (626 nm) and Y7 (841 nm) whereas $PC_{70}BM$ has a strong light absorption in the wavelength range from 300 to 700 nm, indicating the formation of a complementary and broaden absorption spectrum by third components. In addition to the pristine materials, the normalized UV–vis absorption spectra of the blend films are exhibited in Figure 1d. It is observed that the binary films of PM6:Y7 host system, PM6:ITIC-M, and PM6:$PC_{70}BM$ have absorption peaks (λ_{max}) at 817, 694, and 427 nm, respectively, implying that adding $PC_{70}BM$ and ITIC-M as third components may compensate for the absorption of host system. In comparison with binary host PM6:Y7 blend film, a slightly redshifted and increased absorption peak intensity at ≈821 nm in ternary PM6:Y7:ITIC-M blend film is observed, along with an increase shoulder near 730 nm, indicating the contribution from ITIC-M. On the other hand, due to the 10 nm redshifted and increased Y7 absorption peak position in ternary PM6:Y7:$PC_{70}BM$, along with a decrease shoulder near 684 nm, we suspected that $PC_{70}BM$ would have a good compatibility with Y7 to provide more photon absorption which induce a higher short-circuit current density (J_{SC}) values in ternary OSCs.[22]

To confirm the good compatibility of the two acceptors, differential scanning calorimetry (DSC) analysis was performed, as shown in Figure S1, Supporting Information. A melting peak of a $PC_{70}BM$ pure substance appears at 323 °C in the DSC curves and when $PC_{70}BM$ is mixed with Y7, the DSC curves do not show a clear melting peak in Y7:$PC_{70}BM$ blend, indicating that the two acceptors have good miscibility. It is interesting to note that the melting peak of ITIC-M pure substance is difficult to observe in the DSC curve, which is the limitation of the melting point depression method from DSC experiments, especially for those semicrystalline or even amorphous semiconductors, like ITIC-M. Alternatively, miscibility between two acceptors can be estimated by measuring the surface energy. The contact angle measurements of neat films were performed to study the surface tension (γ) of materials and thus to estimate the strength interaction between them and their effect on the phase segregation and blend morphology. **Figure 2** presents the contact angle images based on liquid drops of water and ethylene glycol (EG), while **Table 1** lists the surface tension values of the materials calculated according to Wu's equation and the Flory–Huggins interaction parameter (χ).[23,24] As a result, the surface energies for PM6, Y7, ITIC-M, and $PC_{70}BM$ pristine films are 23.98, 27.23, 28.31, and 28.21 mN m^{-1}, respectively. Accordingly, the interaction parameter χ values between PM6 and Y7 ($\chi_{PM6,Y7} = 0.103$) is relatively small, suggesting a good miscibility between them. In contrast, the values of $\chi_{PM6,ITIC\text{-}M} = 0.180$ and $\chi_{PM6,PCBM} = 0.171$ are higher than those of $\chi_{PM6,Y7}$, indicating a lower miscibility (i.e., weaker interactions) between PM6 host donor and the third components. Interestingly, the interaction parameter between Y7 and the third components are extremely low ($\chi_{Y7,ITIC\text{-}M} = 0.011$ and $\chi_{Y7,PCBM} = 0.009$), indicating a good compatibility between host and guest acceptors which could form an alloy-like composite, supporting our hypothesis. From a thermodynamic point of view, therefore, the addition of a less miscible third component (larger value of χ) relative to the donor effectively increases the pure phase domain sizes, which is favorable for charge dissociation and charge collection.[25]

To investigate the performance of ternary OSC with FA-based $PC_{70}BM$ and NFA-based ITIC-M third components addition, a series of binary and ternary OSCs were fabricated with a conventional device architecture of ITO/PEDOT:PSS/active

Table 1. Contact angles, surface tension, and interaction parameters.

Materials	θ_{water} [°]	θ_{EG} [°]	γ^p [mN m^{-1}]	γ^d [mN m^{-1}]	Surface tension [mN m^{-1}]	$\chi^{a)}$ with PM6	$\chi^{a)}$ with Y7
PM6	92.50	71.68	12.46	11.53	23.98	N/A	0.103
Y7	93.70	64.54	7.77	19.46	27.23	0.103	N/A
ITIC-M	90.91	68.02	19.17	9.14	28.31	0.180	0.011
$PC_{70}BM$	90.60	65.54	17.34	10.86	28.21	0.171	0.009

[a)]The Flory–Huggins interaction parameter based on the surface tension data formula between the donor (D) and the acceptor (A) calculated using $\chi = (\sqrt{\gamma D} - \sqrt{\gamma A})^2$.

layer/PDINO/Ag. The host donor to host acceptor weight ratio was fixed at 1:1, following the optimized conditions for PM6:Y7, and the content of the third components changes proportionally to determine the optimal composition. The detailed device fabrication, characterization, as well as the device optimization of OSCs are described in the Supporting Information and listed in Table S1, Supporting Information. The current density–voltage (J–V) curves for the optimal binary and ternary devices measured under AM1.5G illumination with 100 mW cm^{-2} light intensity are plotted in **Figure 3**a. The comparable results were obtained using different solar simulator and the detailed photovoltaic parameters are listed in **Table 2**. The average performance parameters are obtained from at least 20 individual OSC devices from different batches. The PM6:Y7 binary OSCs deliver a PCE_{max} of 16.46% (average PCE of 16.37% ± 0.39%) with a V_{OC} of 0.845 ± 0.008 V, an impressive J_{SC} of 28.02 ± 0.74 mA cm^{-2}, and an FF of 66.56% ± 1.28%. In contrast, the PM6:ITIC-M binary OSCs show a lower PCE_{max} of 9.22% (average PCE of 8.86 ± 0.25%) with reduced values of J_{SC} (15.86 ± 0.47 mA cm^{-2}) and FF of (54.86% ± 1.24%), but a significantly enhanced V_{OC} of 1.019 ± 0.006 V. Moreover, the PM6:$PC_{70}BM$ binary OSCs exhibit PCE_{max} of 9.43% (average PCE of 8.88% ± 0.32%) with a reduced J_{SC} of 13.51 ± 0.38 mA cm^{-2} but an increased V_{OC} (0.960 ± 0.007 V) and FF (68.33% ± 1.13%). It should be noted that the PM6:Y7 showed the highest efficiency for binary system, which is worth investigated as the high-performing host binary in ternary system. With a minute addition of ITIC-M (10 wt%), the ternary PM6:Y7:ITIC-M OSCs achieved an impressive PCE_{max} of 17.73% (average PCE of 17.15% ± 0.33%) with V_{OC} of 0.868 ± 0.004 V, J_{SC} of 29.27 ± 0.57 mA cm^{-2}, and FF of 67.58% ± 0.89%, outperforming the binary host device.

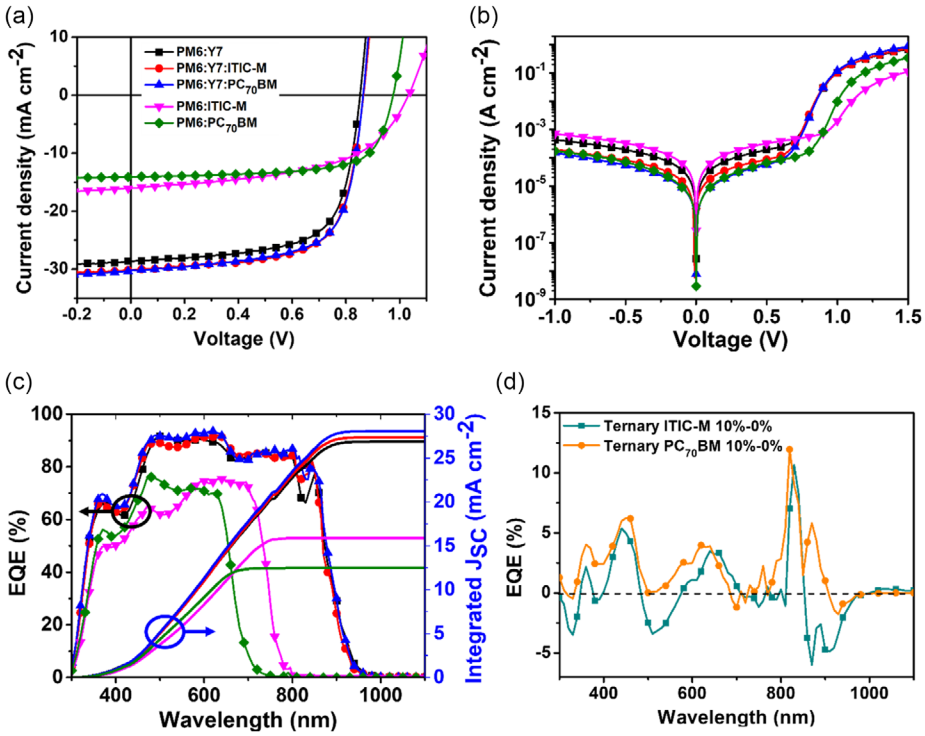

Figure 3. Current density–voltage (J–V) characteristic curves measured under a) AM1.5G illumination and b) in dark condition; c) EQE curves of the corresponding OSCs and d) the ΔEQE values of 10% addition of either ITIC-M or $PC_{70}BM$ with respect to the 0% device.

Table 2. Device performance parameters of optimized binary and ternary OSCs measured under AM1.5G with 100 mW cm^{-2} intensity.

Blend	V_{OC} [V]	J_{SC} [mA cm^{-2}]	$J_{SCavg}{}^{EQE}$ [mA cm^{-2}]	FF [%]	PCE[a]) [%]	E_{loss} [eV]
PM6:Y7 1:1:0	0.850 (0.845 ± 0.008)	28.65 (28.02 ± 0.74)	26.87	67.57 (66.56 ± 1.28)	16.46 (16.37 ± 0.39)	0.539
PM6:Y7:ITIC-M 1:1:0.1	0.870 (0.868 ± 0.004)	30.16 (29.27 ± 0.57)	27.36	67.57 (67.58 ± 0.89)	17.73 (17.15 ± 0.33)	0.490
PM6:Y7:$PC_{70}BM$ 1:1:0.1	0.860 (0.856 ± 0.006)	30.22 (29.38 ± 0.83)	28.05	67.98 (68.39 ± 1.34)	17.67 (17.12 ± 0.34)	0.484
PM6:ITIC-M 1:0:1	1.030 (1.019 ± 0.006)	16.27 (15.86 ± 0.47)	15.87	57.20 (54.86 ± 1.24)	9.22 (8.86 ± 0.25)	0.581
PM6:$PC_{70}BM$ 1:0:1	0.970 (0.960 ± 0.007)	13.91 (13.51 ± 0.38)	12.46	69.93 (68.33 ± 1.13)	9.43 (8.88 ± 0.32)	0.801

[a])The maximum device parameters values are shown outside of parentheses. The statistical values are listed in parentheses, obtained from over 20 individual devices.

The champion ternary device with the addition of ITIC-M benefits from the significant increase of V_{OC} and J_{SC} and slightly improved average FF, mainly related to the upshifted LUMO energy level and complementary absorption of ITIC-M with respect to that of Y7. Besides, loading a small amount of blueshifted absorption third component material, $PC_{70}BM$ (10 wt%), into PM6:Y7 host blend had successfully enhanced the device performance for ternary PM6:Y7:$PC_{70}BM$ device due to the concurrent increase in V_{OC} (0.856 ± 0.006 V), J_{SC} (29.38 ± 0.83 mA cm^{-2}), and FF (68.39 ± 1.34%), thus leading to the high PCE_{max} of 17.67% (average PCE of $17.12\% \pm 0.34\%$). The significant increase of J_{SC} and FF in PM6:Y7:$PC_{70}BM$ device should be attributed to two factors: first, the enhanced photon harvesting of ternary blend due to the broader absorption window that covers the light spectrum from UV to near-infrared (NIR) regions, and the second, the well-developed morphology of ternary blend films with $PC_{70}BM$ addition. As both ternary ITIC-M and ternary $PC_{70}BM$ have similar average PCEs, the V_{OC} and J_{SC} are the main parameters that improve substantially with the addition of third component, which should be benefited from the lower LUMO levels and an alloy-like acceptor phase formation due to good compatibility between the host and guest acceptors. Considering the higher lying LUMO energies in both ITIC-M and ternary $PC_{70}BM$ with regard to Y7, we believe that the energy loss (E_{loss}) can be regulated in the ternary cells. The E_{loss} of OSCs can be determined according to $E_{loss} = E_{gap} - qV_{OC}$ with E_{gap} is the optical energy gap calculated from Tauc's method from the absorption spectra of the blends.[26] As listed in Table 2, the PM6:Y7 binary host OSCs show a E_{loss} of 0.539 eV, consistent to the values in recent study.[21] The E_{loss} of the optimized ternary ITIC-M- and $PC_{70}BM$-based OSCs is 0.490 and 0.484 eV, respectively, which are lower compared to their binary counterparts. The reduced E_{loss} by incorporating appropriate third components is critical in improving performance of ternary OSCs.

Figure 3b presents the dark J–V characteristics of binary and ternary OSCs, which provide an information regarding their bulk and interfacial resistance (R_S), ideality factor along with the leakage current and charge carrier recombination (R_{Sh}) of the devices. The R_S and R_{Sh} (parasitic resistance) and J_0 values of the optimized devices are listed in Table S2, Supporting Information. At reverse voltage bias without illumination ($V < 0$ V), the drift of charge carriers is determined by R_{Sh}, which is correlated with the current loss such as leakage current. The ideal R_{Sh} should be very high, resulting in zero current flows through R_{Sh}, i.e., no current leakage in the device. The R_{Sh} values are 2.75×10^3, 6.20×10^3, and $1.59 \times 10^3\ \Omega\,cm^2$ for PM6:Y7, PM6:Y7:ITIC-M, and PM6:ITIC-M devices, respectively, implying that the leakage current and higher degree of charge carrier recombination in the ternary device can be restrained by incorporating appropriate ITIC-M. The similar tendency to suppress leakage current and lowering the degree of charge carrier recombination can be regulated by adding a proper amount of $PC_{70}BM$ in ternary device, demonstrating by the higher R_{Sh} value of $1.13 \times 10^4\ \Omega\,cm^2$ observed for ternary PM6:Y7:$PC_{70}BM$ device than those of binary host and binary PM6:$PC_{70}BM$ device ($1.07 \times 10^4\ \Omega\,cm^2$). It is worth noting that the high leakage current in ITIC-M-based OSCs leads to a significant reduction about one-order magnitude lower in R_{Sh} values with respect to those of $PC_{70}BM$-based OSCs, which indicates that $PC_{70}BM$ could provide a good interfacial morphology by suppressing the leakage current and morphological traps on the PM6-donor system, better than those of ITIC-M, as discussed later. At high voltages ($V > 1$ V), the charges start to accumulate and are limited by R_S. R_S values are 1.29, 1.41, and $1.19\ \Omega\,cm^2$ for PM6:Y7, PM6:Y7:ITIC-M, and PM6:Y7:$PC_{70}BM$ devices, lower than those R_S values of 4.07 and $1.77\ \Omega\,cm^2$ for PM6:ITIC-M and PM6:$PC_{70}BM$ binary devices, respectively, indicating fewer defects at the Y7-based BHJ blend and/or at the interfaces within the corresponding devices, which should be beneficial for an efficient charge carrier collection and better charge carrier mobility.[12,27] It has been demonstrated that the parasitic resistances effect might contribute to the change of FF in TOSCs, thus we calculated the ideal FF (FF_0) values of all devices along with the FF affected by R_S (FF_{Rs}) and R_{Sh} (FF_{Rsh}), as summarized in Table S3, Supporting Information. In ideal conditions, FF_0s are expected to be improved by the addition of third components; however, the observed experimental FFs are much lower than the calculated ideal FF_0, emphasizing the significant effect of R_S and R_{Sh} on the studied devices.[28]

The other parameter that can be extracted by dark J–V characteristics is the dark reverse saturation current density (J_0) which represents the current density of minority carriers. Suppressing J_0 is an important strategy to increase V_{OC} as V_{OC} is strongly related to J_{ph}/J_0 as described by Equation (1)

$$V_{OC} = \frac{n_{id}kT}{q}\ln\left(\frac{J_{ph}}{J_0} + 1\right) \quad (1)$$

where n_{id} is the ideality factor that can be extracted from either light dependency measurement and transient techniques as mentioned later, k is the Boltzmann constant, T is the temperature, J_{ph} is the photogenerated current, and q is the elementary charge. The extracted J_0 values are 37.00, 7.36, 9.98, 2.03, and 3.96×10^{-9} A cm^{-2} for binary host, ITIC-M ternary, $PC_{70}BM$ ternary, ITIC-M binary, and $PC_{70}BM$ binary devices, respectively. The gradually decreased J_0 values in the studied devices is in excellent agreement with the increased V_{OC} values of ternary OSCs, implying that the J_0 values can be restrained according to the slightly enhanced LUMO levels of alloyed acceptors along with the increased ITIC-M and $PC_{70}BM$ content.

To investigate the underlying reason of the enhanced J_{SC} values, the corresponding external quantum efficiency (EQE) spectra of the relevant OSCs were measured, as presented in Figure 3c. It is observed that the host binary PM6:Y7 has a broad photon response in the wavelength region of 300–950 nm, whereas the binary PM6:ITIC-M and binary PM6:$PC_{70}BM$ show the EQE response in the wavelength of 300–780 nm and 300–730 nm, respectively, which are in good agreement with UV–vis profile. In comparison with binary host device, the optimized ITIC-M-based ternary device exhibits an enhanced EQE responses in the whole wavelength range of 300–830 nm and finely increases in the range of 800–850 nm (see Figure 3d), whereas the optimized $PC_{70}BM$-based ternary device shows an enhanced EQE responses in the whole wavelength of 300–900 nm with a higher response at NIR wavelength (>800 nm). The increased EQE responses for both ternary devices are in good agreement with UV–vis absorption spectra, showing the

simultaneously redshifted λ_{max} of PM6 and Y7 moieties in the ternary blends compared to the corresponding neat films. This result indicates a better molecular orientation of PM6 and Y7 moieties after loading a small amount of compatible third components, thus providing more efficient photocurrent generation. A good agreement between UV–vis and EQE results corroborates the increment in the J_{SC} values of ternary devices with respect to the binary counterparts. In addition, the calculated J_{SC} values from the integrating EQE spectra conform the average J_{SC} values measured from the J–V curves with deviations of less than 10%.

To analyze the effect of the third components addition on the surface morphology of the corresponding blends, we performed the atomic force microscopy (AFM) and transmission electron microscopy (TEM) measurements. The AFM topographic and phase images of binary and ternary blends are presented in **Figure 4**a,b. In the topographic images, the blend films of Y7-, ITIC-M-, and $PC_{70}BM$-based binary blends displayed the root-mean-square (RMS) surface roughness of 1.80, 2.64, and 1.21 nm, respectively. The rougher surfaces of PM6:ITIC-M are undesirable for charge collection by the electrodes, which can be correlated to the highest R_S values among other studied blends, thus PM6:ITIC-M device exhibited the lowest FF value in the J–V characteristic. After loading a small amount of ITIC-M or $PC_{70}BM$, the ternary blend films of PM6:Y7:ITIC-M and PM6:Y7:$PC_{70}BM$ were modified with an optimized RMS roughness of 1.50 and 1.25 nm. As a result, a better dispersity of interpenetrating nanostructure with the favorable shape of the domains in ternary blend films interposed between those of Y7- and ITIC-M/$PC_{70}BM$-based binary blends is observed in the AFM phase images. It is worth noting the smaller RMS and homogeneous nanostructure of $PC_{70}BM$-based binary and ternary blends than those of either Y7-based binary or ITIC-M-based binary and ternary blends may facilitate good interfacial morphology, which in accordance with the lower leakage current observed in dark J–V characteristics. Moreover, the size of the nanofibril structures becomes smaller with increasing ITIC-M contents. The TEM images further corroborate the changes of dispersity in nanoscale blend morphology between binary and ternary blends, as shown in Figure 4c. The homogeneous small domain size and nanofibrous structures can be observed in binary blend films. The fine variation of nanofibrous structures observed from TEM images of the ternary blend suggests the good compatibility among the studied materials. In good agreement with the surface tension calculation, the good compatibility between Y7 and third component ITIC-M/$PC_{70}BM$ is favorable for the acceptor alloy state formation, leading to more efficient electron transport channel.[29]

As widely known in OSCs community, three different fundamental mechanisms are mainly occurred in ternary BHJ: 1) charge-transfer mechanism, where a cascading energy alignment is formed among three components for efficient charge transport and dissociation; 2) energy-transfer mechanism, where the third component with a different bandgap performs as an energy donor, absorbing more photons and inducing long-distance or short-distance energy transfer to the energy acceptor; 3) parallel or alloy mechanism, where the third component either creates additional pathways or mix with the host component and behaves like one tunable material to facilitate charge process.[30] The photoluminescence (PL) measurement can be used as a technique to disregard the charge or energy transfer within the ternary systems. PL spectra of the neat (PM6), binary host (PM6:Y7), and ternary (PM6:Y7:ITIC-M and PM6:Y7:$PC_{70}BM$) films were measured under an excitation wavelength of 600 nm. As plotted in **Figure 5**a, the neat PM6 film exhibits the strongest PL emission. The emission peak at 665 nm of PM6 can be completely quenched in all blend films and in the meantime PL emission peaks of blend films are blueshifted, indicating the presence of an electron transfer between PM6 and the acceptors. The two ternary blend films were more efficiently quenched than the PM6:Y7 binary blend, suggesting the addition of ITIC-M or $PC_{70}BM$ as third component indeed promote electron transfer from PM6 to the mixed acceptor phase. Considering that the overlap between the UV–vis spectral absorption of Y7 and the PL emission of third components

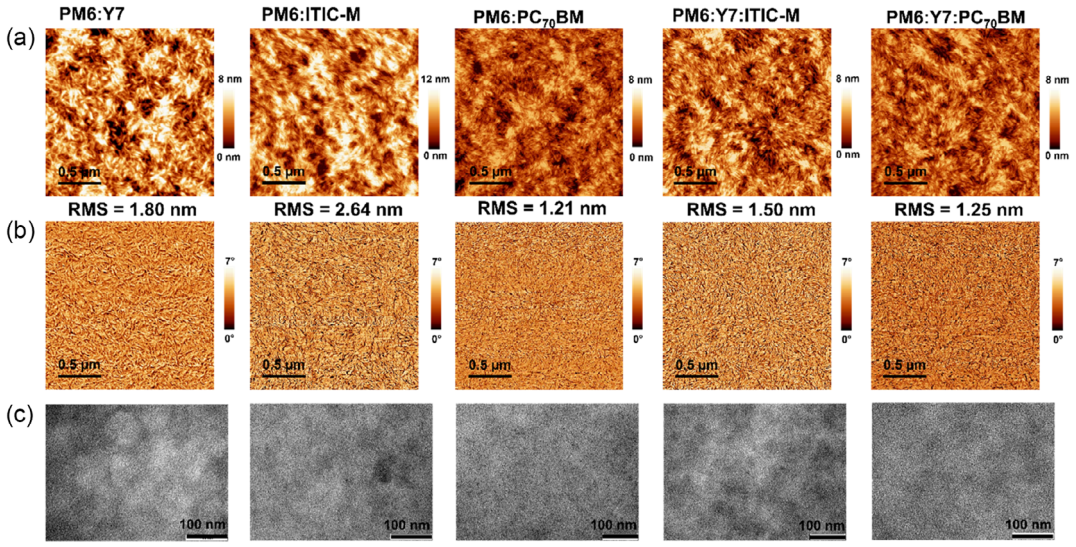

Figure 4. AFM a) topographic and b) phase images and c) TEM images of binary and ternary blend films.

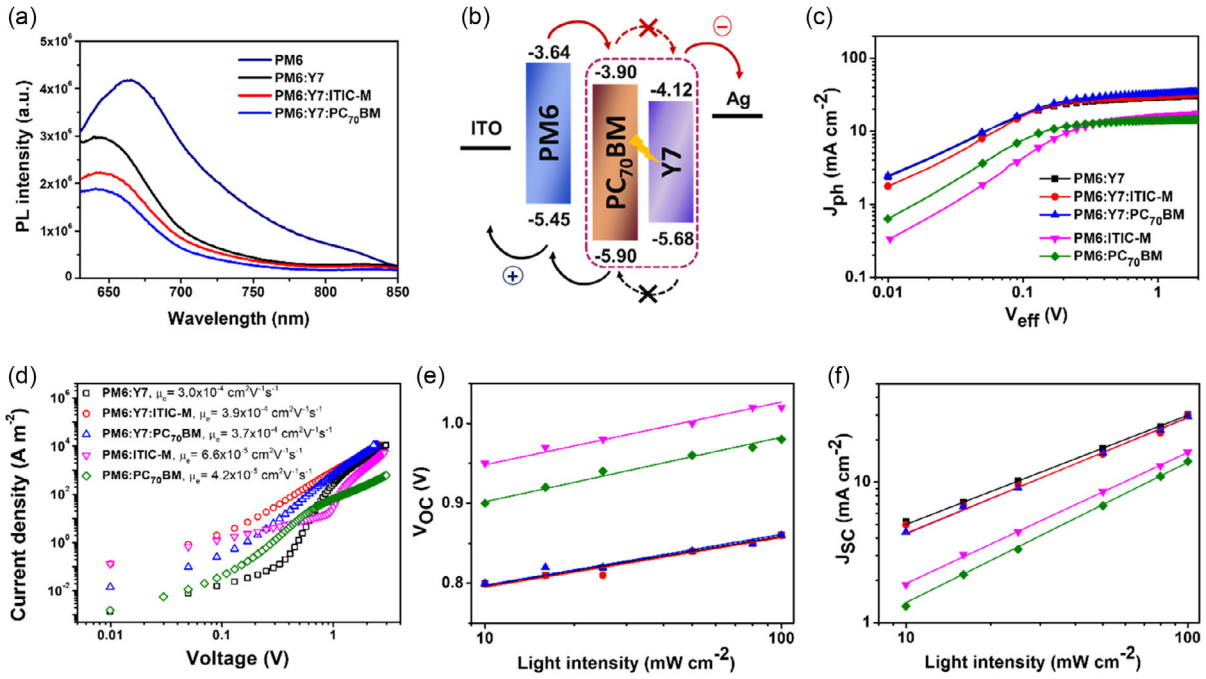

Figure 5. a) PL spectra of Y7-based devices excited at 600 nm; b) energy levels diagram illustrating the ternary working mechanism in our study; c) J_{ph}–V_{eff} curves, d) the electron mobilities, e) V_{OC}, and f) J_{SC} versus light intensity characteristics based on optimized binary and ternary OSCs.

ITIC-M or $PC_{70}BM$ (see Figure S2, Supporting Information), this strongly indicates energy transfer between ITIC-M or $PC_{70}BM$ as energy donor to Y7 as energy acceptor, which could contribute to the slightly increased J_{SC} values and enhanced EQE spectra of ternary OSC devices. Additionally, we fabricated a series of devices with the active layer containing the acceptors-only blends to give further insight on the intermolecular dynamics process between Y7 and the secondary acceptors (ITIC-M or $PC_{70}BM$). Accordingly, the dynamic process between the mixed acceptor alloys should be energy transfer from either ITIC-M or $PC_{70}BM$ to Y7, which may provide an additional route for improving exciton utilization of ternary OSCs. Figure 5b illustrates the working mechanism observed in PM6:Y7:$PC_{70}BM$ ternary OSC, a similar working mechanism is also shown by PM6:Y7:ITIC-M ternary OSC.

As demonstrated above that the extra addition of third components can modify the photovoltaic parameters and blend morphologies, further investigation of charge dynamics in the ternary devices, including charge separation, transport, and collection, is worth studied. First, the photocurrent density (J_{ph}) versus effective voltage (V_{eff}) measurement of the studied devices were performed to gain insight into their exciton dissociation and charge collection. As shown in Figure 5c, J_{ph} for all devices became saturated in the large effective voltage regime ($V_{eff} > 0.5$ V), suggesting that under high applied field, nearly all the excitons could separate and generate free carriers, and then collected by the contacts. The corresponding data are summarized in Table S4, Supporting Information, including the saturated current density (J_{sat}), maximum amounts of absorbed photons (G_{max}), exciton dissociation (η_{diss}), charge collection efficiency (η_{coll}), and dissociation and collection probabilities (P_{diss} and P_{coll}) values. Binary PM6:$PC_{70}BM$ OSCs show the lowest G_{max} value of $8.95 \times 1028\ m^{-3}\ s^{-1}$, consistent with its lowest value of J_{SC}. Higher values of G_{max} implied excellent light harvesting in the devices, which correspond to more efficient exciton generation. The η_{diss} and η_{coll} values as well as P_{diss} and P_{coll} for both $PC_{70}BM$ and ITIC-M-based ternary devices are higher than those of binary host PM6:Y7 OSCs, indicating that the incorporated $PC_{70}BM$ or ITIC-M has a positive effect on the exciton dissociation and charge collection processes, which could be finely associated with the increased of J_{SC} and FF values in the optimized ternary OSCs.

To investigate the influence of incorporating ITIC-M or $PC_{70}BM$ on the electron transport properties of the devices, the electron-only devices with a structure of ITO/ZnO/active layer/PDINO/Ag were fabricated. The electron (μ_e) mobilities were carefully evaluated by a space-charge-limited-current (SCLC) method following the Mott–Gurney model.[31,32] Both ternary blend films of PM6:Y7:ITIC-M and PM6:Y7:$PC_{70}BM$ show higher μ_e values of 3.91×10^{-4} and $3.67 \times 10^{-4}\ cm^2\ V^{-1}\ s^{-1}$, respectively, than those of binary host device ($3.04 \times 10^{-4}\ cm^2\ V^{-1}\ s^{-1}$), as depicted in Figure 5d. Moreover, as the ITIC-M or $PC_{70}BM$ increases, the μ_e values decrease, giving the PM6:ITIC-M and PM6:$PC_{70}BM$ binary blends the μ_e values of 6.62×10^{-5} and $4.21 \times 10^{-4}\ cm^2\ V^{-1}\ s^{-1}$, respectively. The enhanced electron mobility of the ternary blend should facilitate charge transport and suppress charge recombination, which contributes to the higher FF among all the devices in this work. Furthermore, we investigated the electron trap density (N_{trap}) of the corresponding binary and ternary blend films using the following Equation (2)

$$V_{TFL} = \frac{qN_{trap}L^2}{2\varepsilon_r\varepsilon_0} \quad (2)$$

where V_{TFL} is the trap-filled limit voltage evaluated from SCLC measurements as illustrated in Figure S3, Supporting Information, in which q is the elementary charge, L is the thickness of active blend layer, ε_r is the dielectric constant of the blend film, and ε_0 is the vacuum permittivity. It is worth mentioning that the values of the V_{TFL} were diminished for the ternary devices, as listed in the legend of Figure S3, Supporting Information. Moreover, it was interesting to obtain that the ternary devices showed remarkable lower N_{trap} values of 2.13×10^{15} and $1.94 \times 10^{15}\,cm^{-3}$ for the PM6:Y7:ITIC-M and PM6:Y7:$PC_{70}BM$ devices. On the other hand, PM6:Y7, PM6:ITIC-M, and PM6:$PC_{70}BM$ binary devices demonstrated higher N_{trap} values of 6.20×10^{15}, 1.74×10^{16}, and $3.10 \times 10^{15}\,cm^{-3}$, respectively. Accordingly, the increased electron mobility and the decreased electron traps in both ternary devices indicate that the addition of compatible third component in ternary blend passivated the trap states, providing enhanced path for effectively charge carrier transfer and collection with suppressing the recombination mechanisms, explaining their superior P_{diss}, G_{max}, J_{SC} along with their champion PCEs more than the binary ones.

To investigate the charge recombination mechanism in the binary and ternary OSCs, the dependence of V_{OC} and J_{SC} on the various light intensities (P_{light}) was measured according to the corresponding J–V characteristics (see Figure 5e,f and Table S5, Supporting Information). The degree of trap-assisted recombination in the binary and ternary OSCs can be estimated by the variation of V_{OC} as a function of P_{light} described by the relationship $V_{OC} \propto (S2kT/q)\ \ln(P_{light}) \propto (nkT/q)\ \ln(J_{SC})$, where n_{id} stands for the recombination ideality factor of the diode ($n_{id} = S2/S1$), k is the Boltzmann constant, T is the cell temperature in Kelvin, and q is the elementary charge. Generally, the n_{id} values close to 2 reflects the presence of the traps across the active layer and/or at the BHJ/electrode interface, which leads trap-assisted recombination as the major recombination in OSCs.[28] As shown in Figure 5e and Table S5, Supporting Information, the calculated n_{id} values are 1.338, 1.268, and 1.411 for PM6:Y7, PM6:Y7:ITIC-M, and PM6:ITIC-M devices, respectively, which indicates that the trap-assisted recombination can be restrained in the ternary devices by the addition of ITIC-M. Showing similar tendency, n_{id} values of PM6:Y7:$PC_{70}BM$ and PM6:$PC_{70}BM$ are 1.284 and 1.372, respectively, implying that adding $PC_{70}BM$ can make trap-assisted recombination less dominant. In addition, the relationship between J_{SC} and P_{light} can be expressed by the power law, $J_{SC} \propto {P_{light}}^{S1}$, in which $S1$ is the exponential factor referring to bimolecular recombination. Bimolecular recombination can be negligible when $S1$ value is close to unity. As shown in Figure 5f and Table S5, Supporting Information, the fitting $S1$ values are 0.778, 0.822, 0.830, 0.933, and 0.998 for PM6:Y7, PM6:Y7:ITIC-M, PM6:Y7:$PC_{70}BM$, PM6:ITIC-M, and PM6:$PC_{70}BM$, respectively. A stronger deviation of $S1$ from 1 for Y7-based devices indicates that the photocurrent generation for these devices is limited by bimolecular recombination process. It is worth noting that $S1$ values were closer to unity by the addition of ITIC-M or $PC_{70}BM$ as third components, indicating that the guest acceptor components can effectively suppress bimolecular recombination, which is consistent with the improvement of FF of the ternary devices.

To further evaluate the charge recombination dynamics and extraction across the binary and ternary blends in devices, charge extraction (CE), transient photovoltage (TPV), transient photocurrent (TPC), and differential capacitance (DC, combination of TPV/TPC) measurements were performed. DC method is considered as an alternative to charge extraction (CE) technique.[33–36] In brief, the TPC technique measured in the short-circuit condition evaluates the charge present at the solar cell and the TPV in the open-circuit condition examines the charge recombination decay under different light biases.[33] Detail of the experimental description can be found in the Supporting Information. **Figure 6**a shows the charges present under illumination at different open circuit voltages for the PM6:Y7 host binary and PM6:Y7:ITIC-M and PM6:Y7:$PC_{70}BM$ ternary systems. The charges measured in the solar cell were obtained by measuring the capacitance at different light biases: $C(Voc) = \frac{\Delta Q}{\Delta V}$ and finally, the integration of this capacitance gives us an estimation of the charges stored in the cell: $Q(Voc) = \int_0^{Voc} C(Voc)\mathrm{d}Voc$. The obtained curve is mainly formed by two different regimes, first a constant part, attributed to the geometrical capacitance (C_{geo}) and the chemical capacitance (the exponential part) attributed to the charges accumulated at the bulk. Therefore, in order to avoid an incorrect interpretation of the results, the linear part can be fitted and removed from the data, resulting in the solid lines at the bottom. The resulting solid lines show that the charges in the bulk are higher for the ternary systems and so, following the same trend with the corresponding device photocurrent. We can also observe that the slightly shift of voltage at 1 sun conditions agree well with the V_{OC} values obtained for these devices (see **Table 3**). Next, in Figure 6b,c we analyze the ideality factors for the binary and ternary system by using TPC and TPV measurements. As in previous works reported in more detail,[27,37,38] the ideality factor (n_{id}) can be also obtained by using the following expressions

$$n = n_0 \times \exp\left(\frac{qVoc}{n_n kT}\right) \quad (3)$$

$$\tau_{\Delta n} = \tau_{\Delta n_0} \times \exp\left(\frac{qVoc}{n_\tau kT}\right) \quad (4)$$

and where the parameters γ and β obtained from Figure 6b,c are defined as $\gamma = \frac{q}{n_n kT}$ and $\beta = \frac{q}{n_\tau kT}$, respectively. Finally, the n_{id} can be calculated by using the equation $n_{id}^{-1} = n_n^{-1} + n_\tau^{-1}$. Table 3 shows all the parameters obtained through TPC/TPV and the comparison with the ideality factors obtained with the J–V characteristics. Although two different techniques were employed, the n_{id} values from J–V characteristics and from TPC/TPV techniques are found to be identical for our solar cells. The identical ideality factor values has been reported in our previous work and other authors with respect to the steady-state values.[27,39,40] As a result, the good agreement of steady state and transient techniques demonstrates the validity of the Shockley model to studying the recombination and diode behavior for ternary organic solar cells. In addition, the recombination kinetics were evaluated by

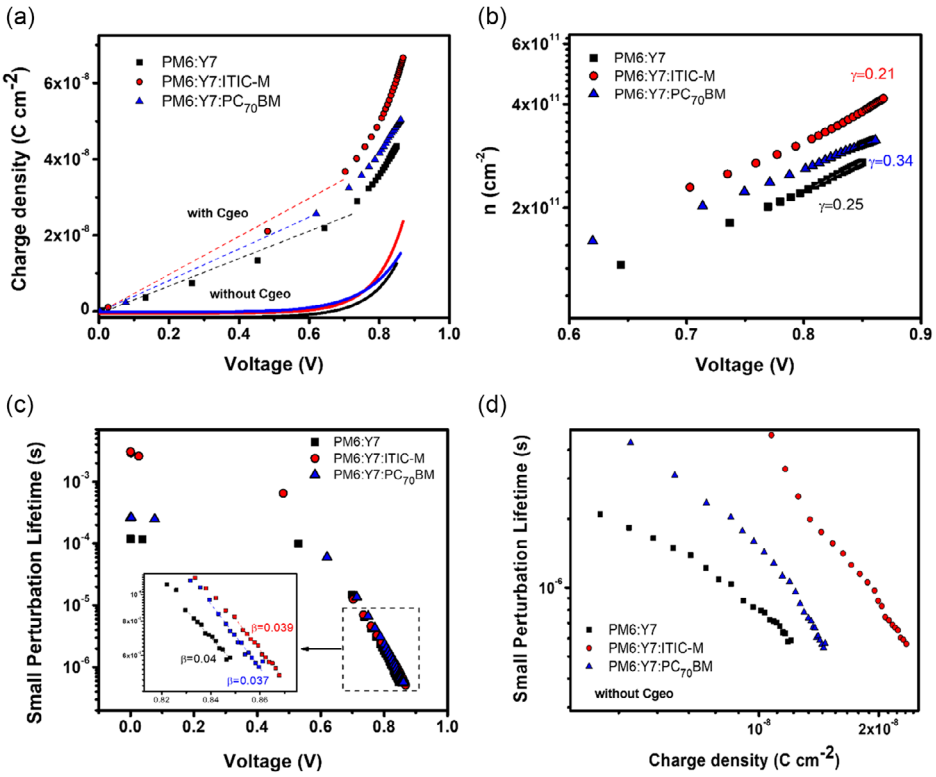

Figure 6. a) Charge density as a function of V_{OC} for the binary and ternary systems; b) charge (n) versus voltage with the n_n fitting (γ). c) Small perturbation lifetime versus voltage with the n_τ fitting (β). d) Small perturbation lifetime plot as a function of charge density without the geometrical capacitance.

Table 3. Summary of the ideality factors obtained by TPC/TPV techniques and *J–V* characteristics.

Blend system	n_n	n_τ	n_{id} (TPC/TPV)	n_{id} (*J–V*)
PM6:Y7	9.76	1.54	1.34	1.34
PM6:Y7:ITIC-M	8.12	1.78	1.26	1.27
PM6:Y7:$PC_{70}BM$	13.39	1.43	1.29	1.28

plotting the small perturbation lifetime—obtained by TPV—as a function of charge density—obtained by DC—as shown in Figure 6d. Clearly, for the same number of charges, the binary system presents faster recombination in comparison to the ternary systems. These results imply that the third component can contribute to more effective extraction of charges and a retardation in charge recombination losses, which also implies higher J_{sc}, V_{OC}, FF and thus improving the overall cell performance.[41–43]

To gain deeper insight into the process involved by incorporating $PC_{70}BM$ or ITIC-M as third component in ternary blends, impedance spectroscopy (IS) was employed to measure the capacitance–frequency (*C–f*) and capacitance–voltage (*C–V*) characteristics of solar cells. In order to extract charge carrier accumulation and/or interfacial charge transfer information, the IS measurement should be carried out under open-circuit condition and equivalent circuits are often modeled to fit the experimental data.[44,45] **Figure 7**a,b shows the Cole–Cole plots for binary host, ITIC-M- and $PC_{70}BM$-ternary solar cells measured at open-circuit bias voltage under constant illumination of 1 sun with frequency ranging from 5 kHz to 10 MHz. A typical arc behavior with one semicircle is observed for all samples, indicating the presence of different RC components in the spectra. Arredondo et al. proposed that the low-frequency arc is ascribed to the charge accumulation that cannot be extracted by the device contacts.[46] The smaller arc radius and lower impedance at low frequency observed for both ITIC-M- and $PC_{70}BM$-based ternary devices suggest that ternary strategy could suppress the charge accumulation impact that could be originated from surface morphology disorder of the blend.[47] These results are coherent with the lower RMS and low leakage current and as a sequence, better device performance of both ternary devices compares to those of binary ones. Similar behavior was obtained for the binary host and ternary devices at maximum power point voltage (V_{MPP}) and short-circuit current voltage ($V = 0$ V) bias, as shown in Figure S4, Supporting Information.

To understand in which layer the accumulation is taking place, an equivalent circuit model comprising one series resistance (R_S) connected in series with three resistor/capacitor components (3RC) with Debye model was employed to fit the experimental *Z'–Z''* data (see inset of Figure 7a). The solid lines are the fitting curves and the fitted parameters of the 3RC + Debye equivalent circuit are listed in Table S6, Supporting Information. R_S represents the series resistance from the metallic wires and the ohmic components such as ITO layer or Ag electrodes[48] and L is the added inductor to eliminate the impact of the connecting line

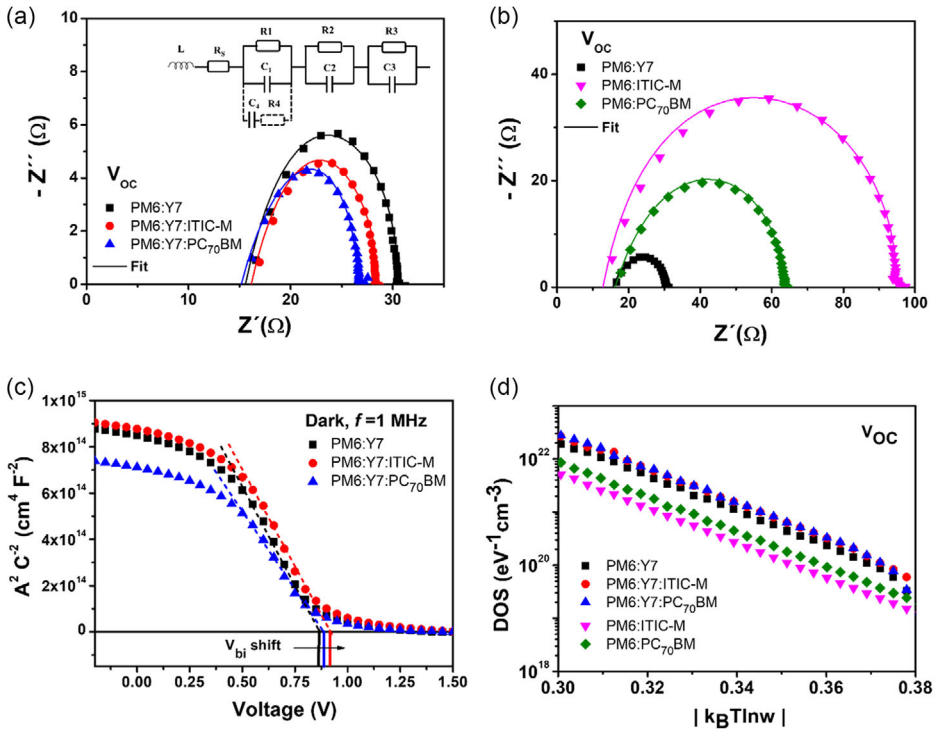

Figure 7. a) Cole–Cole plot of binary host and ternary OSCs and b) Cole–Cole plot of binary OSCs; c) Mott–Schottky curve of at 1 MHz under dark condition; and d) density of states (DOS) plot as a function of $|k_BT\ln\omega|$ at V_{OC} under AM1.5G illumination for binary and ternary OSCs.

during high-frequency scanning.[44,49] A distributed resistor (R) in 3RC elements represents the resistance of electron transport in each layer where R_1, R_2, and R_3 refer to PEDOT:PSS, blend active layer, and the PDINO layer, respectively. It is important to note that the capacitance (C) corresponds to the geometrical capacitance calculated from each layer, which can be expressed by $C_g = \frac{\varepsilon_0\varepsilon_r}{A}$. Notably, an extra impeded R_4 and C_4 in series that attached in parallel with R_1 and C_1 is following the Debye model to explain the effect of the effect of third component introduction in ternary blends. As shown in Table S6, Supporting Information, the values of C_1, C_2, and C_3 are constant for all devices, coherent with the theoretical values shown in Table S7, Supporting Information. This might imply that at V_{OC}, the impedance response was controlled by the geometrical capacitances provided by the metal–insulator–metal (MIM) model portraying the presence of fully depleted layers.[50] Compared to R_1 and R_2 values, the R_3 values of binary host and ternary devices are onefold higher and contribute more to the total resistance (R_{total}) of the corresponding devices, as depicted in Figure S5, Supporting Information. It suggests that the electrical properties of Y7-based binary and ternary devices were mainly controlled by the charge accumulation at the cathode interface (active layer/PDINO). Moreover, the total contribution of R_{total} originated from the contribution of R_2 values in binary ITIC-M and binary $PC_{70}BM$ is more pronounced by higher amount third component introduced to the system, which means that the charges cannot be easily extracted due to the higher guest components content in the active layers. This trend of the resistance obtained for the devices was confirmed by the Bode plot curves in Figure S6, Supporting Information. It is interesting to find that the R_1, R_2, R_3 and thus R_{total} values for ITIC-M- or $PC_{70}BM$-ternary devices are smaller than the binary devices, which can well explain the simultaneously increased J_{SC} and FF in the optimized ternary devices that agree well with J–V characteristic, EQE, PL, surface analysis and TPV measurements.

In addition, impedance spectroscopy can be applied to investigate the effect of third component addition on the energetic disorder of transport site in ternary blends by C–V analysis. Figure 7c shows the Mott–Schottky plots for binary host, ITIC-M-based, and $PC_{70}BM$-based ternary OSCs from which the built-in potential (V_{bi}) can be extracted by the intercept of the curve with x-axis. The calculated V_{bi} from the C–V analysis was recorded in the dark at frequency of 1 MHz. The obtained V_{bi} values were 0.865, 0.915, and 0.885 V for binary host, ITIC-M ternary, and $PC_{70}BM$ ternary OSCs, respectively. It is observed that V_{bi} values increase after the addition of the third component. The increasing V_{bi} values are also observed in binary ITIC-M and binary $PC_{70}BM$ OSCs, as shown in Figure S7, Supporting Information. With the larger V_{bi}, a wider depletion region would be formed, resulting in improved separation of charge carries and reduced bulk recombination.[51] As a consequence, the influence of the electric field in device with larger V_{bi} yields to the higher V_{OC} of both ternary devices.

The defects density can be evaluated from the capacitance–frequency (C–f) measurement to calculate the trap density of state (DOS) at a given energy level, E_ω, by the variation of the capacitance of the device with the frequency, as described by Equation (5)

$$\mathrm{DOS}(E_\omega) = -\frac{V_{\mathrm{bi}}\omega}{tqTk_{\mathrm{B}}}\frac{\partial \mathrm{C}}{\partial \omega} \quad (5)$$

where C is the measured capacitance, V_{bi} is the built-in potential, ω is the angular frequency, t is the layer thickness, k_{B} is the Boltzmann constant, q is the electron charge, and T is room temperature in Kelvin. The assumption in Equation (5) is that the variations in the capacitance of the devices with frequency are correlated to the trapping and the charge release by shallow traps in the bandgap near to the Fermi energy level.[52,53] To observe the relation of the trap-DOS as an energy dependent, the following equation has been applied

$$(E_\omega)_{\mathrm{traps}} = k_{\mathrm{B}}T\ln\frac{2\beta N}{\omega} = E_{\mathrm{O}} - k_{\mathrm{B}}T\ln\omega \quad (6)$$

where β is the cross section and N is the effective density of state.[54] Assuming that $2\beta N = X$ is independent of the frequency value, the change in its value is related to the shift in the DOS values on energy scale ($E_{\mathrm{O}} = k_{\mathrm{B}}T\ln(2\beta N)$). Figure 7d displays the calculated trap-DOS plotted as a function of energy for the fabricated devices. A single exponential trap distribution for all samples is observed with almost the same slope values, which defines the same trap activation energy and carrier response.[55] Interestingly, after the introduction of either ITIC-M or $PC_{70}BM$ into the binary host blend, a shift in E_{O} values was observed, showing a slight increase density of defects. As explained by Equation (6), the higher shift of E_{O} or higher DOS values could be originated from the decrease in the βN value, indicating a higher obtained energy due to the less-localized shallow trap sites created by adding a small amount of the appropriate third components. In addition, Figure S8, Supporting Information, is shown to further quantify the energy shifting values of the corresponding ternary OSCs with respect to the binary host according to equation 4. It is noticed that the PM6:Y7 binary OSC exhibits higher trapping sites than those of ternary OSCs, confirming the higher performance of ternary OSCs due to the addition of ITIC-M or $PC_{70}BM$ that minimized the present of defects inside the ternary devices. It is interesting that the less-localized shallow trap sites in ternary blends is in highly accordance with the calculated Urbach energy, as shown in Figure S9, Supporting Information, and described by Equation (7)

$$\alpha(E) = \alpha_0 e^{(E-E_{\mathrm{g}})/E_{\mathrm{U}}} \quad (7)$$

where $\alpha(E)$ is the optical absorption coefficient, α_0 is the optical absorption coefficient at the band edge, E is the photon energy, and E_{U} is the Urbach's energy. The E_{U} represents the DOS distribution, which explains the energetic disorder in the molecular orbital. The calculated E_{U} were 27.99, 27.28, and 25.81 meV, respectively, for PM6:Y7-, PM6:Y7:ITIC-M-, and PM6:Y7:$PCP_{70}BM$-based OSCs, indicating the lower energetic disorder can be achieved by the introduction of higher lying LUMO energy and morphology compatible of third components in the ternary devices.

3. Conclusions

In summary, a series of OSCs were prepared with PM6 as host donor, Y7 as host acceptor, and ITIC-M or $PC_{70}BM$ as guest acceptors. Despite the fact that the two acceptor guests $PC_{70}BM$ and ITIC-M have completely different chemical structures, they possess common properties such as excellent miscibility and higher LUMO energy level in comparison to the host acceptor, resulting in an improved PCE from 16.46% (PM6:Y7 binary OSCs) to high PCEs of 17.73% (ITIC-M-based ternary OSCs) and 17.67% ($PC_{70}BM$-based ternary OSCs). By intensively investigating charge transport, charge extraction and charge recombination properties in ternary OSCs, we found that the ITIC-M and $PC_{70}BM$ guest acceptors exhibit excellent compatibility with the host acceptor Y7, such that well-mixed acceptor phases are formed in the ternary blends. The higher LUMO levels of the third components help the ternary OSCs elevate the V_{OC} by reducing energy-loss and reverse saturation current, creating less-localized shallow trap sites along with suppressing charge recombination and Urbach energy. Furthermore, photoluminescence and single material device investigations demonstrate energy transfer between the two well-mixed acceptors, contributing to more efficient exciton dissociation and electron transport, thus increasing J_{SC}. The combination of these improvements leads in a simultaneously enhanced V_{OC}, J_{SC}, and FF with respect to those of binary host. Our findings demonstrate that a good compatibility between the guest and host acceptors with suitable energy levels to achieve complementary absorption are the keys to realize synergistically modified nanomorphology and photophysical processes toward high-efficiency ternary organic solar cells.

Supporting Information

Supporting Information is available from the Wiley Online Library or from the author.

Acknowledgements

A.A.A.T. acknowledges the financial support from the European Union's Horizon 2020 research and innovation program under the Marie Skłodowska-Curie grant agreement no. 713679. This work was further supported by the Spanish Ministerio de Ciencia, Innovación y Universidades (MICINN/FEDER) PDI2021-128342OB-I00, by the Agency for Management of University and Research Grants (AGAUR) ref. 2021-SGR-00739, by Diputació de Tarragona 2022PGR-DIPTA-URV04, and from the Catalan Institution for Research and Advanced Studies (ICREA) under the ICREA Academia Award. ICIQ and ICREA are also acknowledged for its contribution with the photoluminescence spectra, transient photoinduced measurements, and discussion of the results.

Conflict of Interest

The authors declare there is no conflict of interest.

Data Availability Statement

The data that support the findings of this study are available from the corresponding author upon reasonable request.

Keywords

alloy-like models, fullerenes, impedance spectroscopy, nonfullerenes, ternary organic solar cells, transient photovoltage

Received: March 24, 2023
Published online: April 19, 2023

[1] Y. Cui, Y. Xu, H. Yao, P. Bi, L. Hong, J. Zhang, Y. Zu, T. Zhang, J. Qin, J. Ren, Z. Chen, C. He, X. Hao, Z. Wei, J. Hou, *Adv. Energy Mater.* **2021**, *11*, 2100079.
[2] K. Yu, W. Song, Y. Li, Z. Chen, J. Ge, D. Yang, J. Zhang, L. Xie, C. Liu, Z. Ge, *Small Struct.* **2021**, *2*, 2100099.
[3] X. Chen, D. Wang, Z. Wang, Y. Li, H. Zhu, X. Lu, W. Chen, H. Qiu, Q. Zhang, *Chem. Eng. J.* **2021**, *424*, 130397.
[4] Q. Liu, Y. Jiang, K. Jin, J. Qin, J. Xu, W. Li, J. Xiong, J. Liu, Z. Xiao, K. Sun, S. Yang, X. Zhang, L. Ding, *Sci. Bull.* **2020**, *65*, 272.
[5] Y. Zhang, G. Li, *Acc. Mater. Res.* **2020**, *1*, 158.
[6] A. A. A. Torimtubun, J. Follana-Berná, J. G. Sanchez, J. Pallarés, Á. Sastre-Santos, L. F. Marsal, *ACS Appl. Energy Mater.* **2021**, *4*, 5201.
[7] C. Zhao, J. Wang, X. Zhao, Z. Du, R. Yang, J. Tang, *Nanoscale* **2021**, *13*, 2181.
[8] Q. An, F. Zhang, J. Zhang, W. Tang, Z. Deng, B. Hu, *Energy Environ. Sci.* **2016**, *9*, 281.
[9] N. Y. Doumon, L. Yang, F. Rosei, *Nano Energy* **2022**, *94*, 106915.
[10] N. Gasparini, A. Salleo, I. McCulloch, D. Baran, *Nat. Rev. Mater.* **2019**, *4*, 229.
[11] E. Moustafa, A. A. A. Torimtubun, J. Pallarès, L. F. Marsal, *Sol. RRL* **2021**, *6*, 2100480.
[12] B.-H. Jiang, Y.-P. Wang, C.-Y. Liao, Y.-M. Chang, Y.-W. Su, R.-J. Jeng, C.-P. Chen, *ACS Appl. Mater. Interfaces* **2021**, *13*, 1076.
[13] H. Huang, X. Li, S. Chen, B. Qiu, J. Du, L. Meng, Z. Zhang, C. Yang, Y. Li, *J. Mater. Chem. A* **2019**, *7*, 27423.
[14] K. N. Zhang, Z. N. Jiang, T. Wang, M. S. Niu, L. Feng, C. C. Qin, S. K. So, X. T. Hao, *Sol. RRL* **2020**, *4*, 2000165.
[15] Q. An, J. Wang, W. Gao, X. Ma, Z. Hu, J. Gao, C. Xu, M. Hao, X. Zhang, C. Yang, F. Zhang, *Sci. Bull.* **2020**, *65*, 538.
[16] Z. Jia, Z. Chen, X. Chen, L. Bai, H. Zhu, Y. M. Yang, *J. Phys. Chem. Lett.* **2021**, *12*, 151.
[17] M. A. Pan, T. K. Lau, Y. Tang, Y. C. Wu, T. Liu, K. Li, M. C. Chen, X. Lu, W. Ma, C. Zhan, *J. Mater. Chem. A* **2019**, *7*, 20713.
[18] Y. Dong, Y. Zou, J. Yuan, H. Yang, Y. Wu, C. Cui, Y. Li, *Adv. Mater.* **2019**, *31*, 1904601.
[19] K. N. Zhang, J. J. Guo, L. J. Zhang, C. C. Qin, H. Yin, X. Y. Gao, X. T. Hao, *Adv. Funct. Mater.* **2021**, *31*, 2100316.
[20] L. Zhan, S. Li, T. K. Lau, Y. Cui, X. Lu, M. Shi, C. Z. Li, H. Li, J. Hou, H. Chen, *Energy Environ. Sci.* **2020**, *13*, 635.
[21] Y. Cui, H. Yao, J. Zhang, T. Zhang, Y. Wang, L. Hong, K. Xian, B. Xu, S. Zhang, J. Peng, Z. Wei, F. Gao, J. Hou, *Nat. Commun.* **2019**, *10*, 2515.
[22] X. Wang, L. Zhang, L. Hu, Z. Xie, H. Mao, L. Tan, Y. Zhang, Y. Chen, *Adv. Funct. Mater.* **2021**, *31*, 2102291.
[23] S. Wu, *J. Polym. Sci. Part C* **1971**, *34*, 19.
[24] M. Tambasco, J. E. G. Lipson, J. S. Higgins, *Macromolecules* **2006**, *39*, 4860.
[25] R. Ma, T. Liu, Z. Luo, K. Gao, K. Chen, G. Zhang, W. Gao, Y. Xiao, T. K. Lau, Q. Fan, Y. Chen, L. K. Ma, H. Sun, G. Cai, T. Yang, X. Lu, E. Wang, C. Yang, A. K. Y. Jen, H. Yan, *ACS Energy Lett.* **2020**, *5*, 2711.
[26] C. Yan, R. Ma, G. Cai, T. Liu, J. Zhu, J. Wang, Y. Li, J. Huang, Z. Luo, Y. Xiao, X. Lu, T. Yang, X. Zhan, H. Yan, G. Li, *EcoMat* **2020**, *2*, e12061.
[27] A. A. A. Torimtubun, M. Méndez, J. G. Sánchez, J. Pallarès, E. Palomares, L. F. Marsal, *Sustainable Energy Fuels* **2021**, *5*, 6498.
[28] A. A. A. Torimtubun, J. G. Sánchez, J. Pallarès, L. F. Marsal, *Sustainable Energy Fuels* **2020**, *4*, 3378.
[29] X. Ma, J. Wang, J. Gao, Z. Hu, C. Xu, X. Zhang, F. Zhang, *Adv. Energy Mater.* **2020**, *10*, 2001404.
[30] Y. Chang, J. Zhang, Y. Chen, G. Chai, X. Xu, L. Yu, R. Ma, H. Yu, T. Liu, P. Liu, Q. Peng, H. Yan, *Achieving Efficient Ternary Organic Solar Cells Using Structurally Similar Non-Fullerene Acceptors With Varying Flanking Side Chains*, Vol. *11*, John Wiley and Sons Inc, **2021**.
[31] J. A. Röhr, D. Moia, S. A. Haque, T. Kirchartz, J. Nelson, *J. Phys. Condens. Matter* **2018**, *30*, 105901.
[32] S. A. Moiz, I. A. Khan, W. A. Younis, K. S. Karimov, *Conducting Polymers*, Intechopen **2016**, http://dx.doi.org/10.5772/63527.
[33] E. Palomares, N. F. Montcada, M. Méndez, J. Jiménez-López, W. Yang, G. Boschloo, in *Characterization Techniques for Perovskite Solar Cell Materials*, **2019**, pp. 161–180, https://doi.org/10.1016/B978-0-12-814727-6.00007-4.
[34] C. Rodríguez-Seco, M. Méndez, C. Roldán-Carmona, R. Pudi, M. K. Nazeeruddin, E. J. Palomares, *Angew. Chem. Int. Ed.* **2020**, *59*, 5303.
[35] N. F. Montcada, M. Méndez, K. T. Cho, M. K. Nazeeruddin, E. Palomares, *Nanoscale* **2018**, *10*, 6155.
[36] J. W. Ryan, E. Palomares, J. W. Ryan, E. Palomares, *Adv. Energy Mater.* **2017**, *7*, 1601509.
[37] C. G. Shuttle, B. O'Regan, A. M. Ballantyne, J. Nelson, D. D. C. Bradley, J. De Mello, J. R. Durrant, *Appl. Phys. Lett.* **2008**, *92*, 093311.
[38] T. Kirchartz, J. Nelson, *Phys. Rev. B Condens. Matter Mater. Phys.* **2012**, *86*, 165201-1.
[39] D. Kiermasch, L. Gil-Escrig, A. Baumann, H. J. Bolink, V. Dyakonov, K. Tvingstedt, *J. Mater. Chem. A* **2019**, *7*, 14712.
[40] D. Kiermasch, A. Baumann, M. Fischer, V. Dyakonov, K. Tvingstedt, *Energy Environ. Sci.* **2018**, *11*, 629.
[41] A. Yin, D. Zhang, J. Wang, H. Zhou, Z. Fu, Y. Zhang, *Front. Chem.* **2020**, *8*, 21.
[42] M. Privado, P. de la Cruz, G. Gupta, R. Singhal, G. D. Sharma, F. Langa, *Sol. Energy* **2020**, *199*, 530.
[43] R. Sharma, H. Lee, M. Seifrid, V. Gupta, G. C. Bazan, S. Yoo, *Sol. Energy* **2020**, *201*, 499.
[44] E. Von Hauff, *J. Phys. Chem. C* **2019**, *123*, 11329.
[45] E. Osorio, J. G. Sa, L. N. Acquaroli, M. Pacio, J. Ferre, L. F. Marsal, *ACS Omega* **2017**, *2*, 3091.
[46] B. Arredondo, M. B. Martín-López, B. Romero, R. Vergaz, P. Romero-Gomez, J. Martorell, *Sol. Energy Mater. Sol. Cells* **2016**, *144*, 422.
[47] M. B. Upama, N. K. Elumalai, M. A. Mahmud, M. Wright, D. Wang, C. Xu, A. Uddin, *Sol. Energy Mater. Sol. Cells* **2018**, *176*, 109.
[48] E. Moustafa, J. G. Sánchez, L. F. Marsal, J. Pallarès, *ACS Appl. Energy Mater.* **2021**, *4*, 4099.
[49] J. Gao, X. Ma, C. Xu, X. Wang, J. H. Son, S. Y. Jeong, Y. Zhang, C. Zhang, K. Wang, L. Niu, J. Zhang, H. Y. Woo, F. Zhang, *Chem. Eng. J.* **2022**, *428*, 129276.
[50] H. Schroeder, *J. Appl. Phys.* **2015**, *117*, 215103.
[51] Y. Zhu, T. Song, F. Zhang, S. T. Lee, B. Sun, *Appl. Phys. Lett.* **2013**, *102*, 113504.

[52] B. Ecker, J. C. Nolasco, J. Pallarés, L. F. Marsal, J. Posdorfer, J. Parisi, E. Von Hauff, *Adv. Funct. Mater.* **2011**, *21*, 2705.
[53] H. F. Haneef, A. M. Zeidell, O. D. Jurchescu, *J. Mater. Chem. C* **2020**, *8*, 759.
[54] T. Walter, R. Herberholz, C. Müller, H. W. Schock, *J. Appl. Phys.* **1996**, *80*, 4411.
[55] G. Garcia-Belmonte, A. Munar, E. M. Barea, J. Bisquert, I. Ugarte, R. Pacios, *Org. Electron.* **2008**, *9*, 847.